Numerical assessment of failure mechanisms in fibre metal laminates

Frank Hashagen and René de Borst
Delft University of Technology, Koiter Institute Delft, P.O. Box 5048, 2600 GA Delft,
The Netherlands, email: F.Hashagen@CT.tudelft.nl

In this contribution numerical models are discussed for describing failure mechanisms in fibre metal laminates. Fibre metal laminates form a new class of materials which are considered for a possible application to the fuselage of future aircraft generations. The intensive experimental analyses of these materials are focused on the assessment of their residual strength and on the assessment of new design methods. To support the experimental analyses numerical models are used to describe cracking and delamination in fibre metal laminates. A special continuum element and a corresponding interface element are introduced. Furthermore, loading functions are applied which account for cracking and delamination. Subsequently, results are discussed which are obtained from numerical analyses of the residual strength of plates made of GLARE™ . Finally, the splicing technique as a new design method is assessed by a comparison between numerical and experimental results.

Key words: **fibre metal laminates, solid-like shell, interface elements, crack growth, residual strength, delamination, splices**

1 Description of fibre metal laminates

Fibre metal laminates are bonded arrangements of thin aluminium layers and prepreg layers that are reinforced either by glass fibres or by aramid fibres, Figure 1. They have been pioneered at the Faculty of Aerospace Engineering of Delft University of Technology. Due to its fatigue resistance and fracture characteristics the fibre metal laminate GLARE™ shows a high potential to serve as skin material for the fuselage of a new super large aircraft, the AIRBUS A3XX. However, before fibre metal laminates can be applied intensive testing is necessary to evaluate the characteristics of the material and to derive the corresponding material parameters. Furthermore, fibre metal laminates offer the possibility to apply new design methods which make use of their layered structure. Commonly, the fuselage of an aircraft is composed of a number of aluminium sheets. Their width determines the number of joints that add to the structural weight of the fuselage. By applying the so-called splicing technique the width of the sheets can be increased which subsequently reduces the weight of the structure.

Due to the economical interest in fibre metal laminates and their possible application to the fuselage of the A3XX the experimental research is carried out under strict time and cost constraints. Since testing is time consuming and expensive numerical strategies are necessary to enhance the development of fibre metal laminates. Furthermore, the complex structure of the material requires a

theoretical verification of the results that are obtained applying design methods which are derived for homogeneous materials. Especially the residual strength (strength of the material in the presence of cracks) and the impact of the splicing technique are major points of concern [10].
For the derivation of the numerical models several aspects must be taken into consideration. First, a continuum element is derived. It is imperative that the continuum element describes fibre metal laminates in a three-dimensional state. This goal is achieved with a solid-like shell element. Secondly, interface elements are applied at the locations where cracking or delamination is expected to occur. They are consistent to the formulation of the continuum elements. Thirdly, the failure mechanisms cracking and delamination must be accounted for. Here, cracking determines the residual strength of the fibre metal laminates and delamination has a significant impact on spliced structures. Both mechanisms are described by applying interface elements and introducing a loading function which bounds all states of the stress in the interface elements.
In the following the continuum element and the interface element are introduced briefly. Subsequently, the interface crack model is described and applied for a residual strength analysis of a centre cracked plate made of the fibre metal laminate GLARE™. Finally, the impact of splices is studied with spliced tension specimen made of GLARE™ .

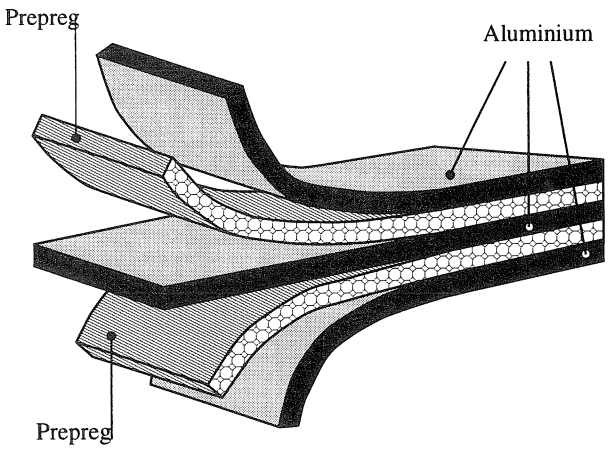

Fig. 1. Schematic sketch of the lay-up of fibre metal laminates.

2 Applied finite elements

2.1 *Solid-like shell element*

Typically, structures made of fibre metal laminates are very thin. For these applications shell elements are widely used in finite element calculations. However, the description of delamination in a three-dimensional manner is difficult with shell elements. The reason lies in the separation of the different layers when delamination occurs. This is often accompanied by strains and stresses in the thickness direction which are not incorporated in most shell theories. Alternatively, solid

elements can be applied. However, these elements tend to lock in thin applications. Hence, a new class of elements, so-called solid-like shell elements [4, 12], is applied to describe fibre metal laminates. An eight-noded and a sixteen-noded solid-like shell element are derived. The sixteen-noded solid-like shell element is displayed in Figure 2. In addition to the geometrical nodes 1-16, four internal nodes are defined in the middle of the four corners of the element. Through the location of the nodes an isoparametric frame of reference is spanned, $\Theta = (\xi, \eta, \zeta)$. In the undeformed state each material point **X** in the element can be written as a function of the isoparametric coordinates (ξ_m, η_m, ζ_m):

$$\mathbf{X} = \mathbf{X}^0(\xi_m, \eta_m) + \zeta_m \mathbf{D}(\xi_m, \eta_m) \tag{1}$$

In eq.(1) the vector $\mathbf{X}^0$ represents the projection of the material point onto the mid-surface of the element. The vector $\boldsymbol{D}$ represents the thickness director in this point, see Figure 3. The position **x** of the same material point in the deformed configuration equals: $\boldsymbol{x} = \boldsymbol{X} + \boldsymbol{u}$, in which the displacement field $\boldsymbol{u}$ reads:

$$\boldsymbol{u} = \boldsymbol{u}^0 + \zeta_m \boldsymbol{u}^1 + (1 - \zeta_m^2)\boldsymbol{w} \tag{2}$$

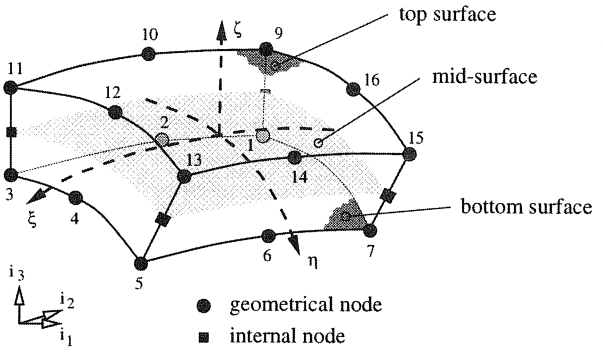

Fig. 2. Geometry of the sixteen-noded solid-like shell element.

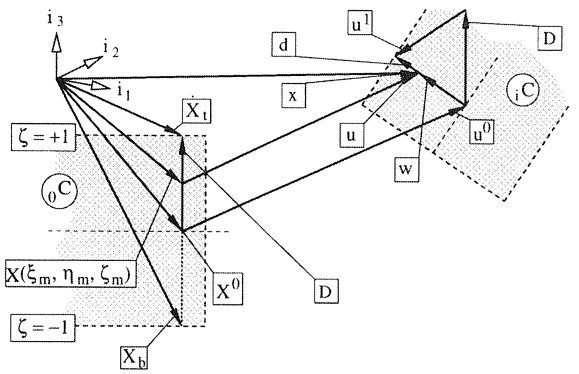

Fig. 3. Kinematics of the sixteen-noded solid like shell element.

The component u^0 denotes the deformation of the projection onto the mid-surface, the component u^1 represents the deformation of the thickness director and w stands for the internal stretching which is colinear to the thickness director $d = D + u^1$ of the deformed configuration. Applying this formulation a linear strain in the thickness direction is assured. As a result, so-called "Poisson-Thickness-Locking" [3] is avoided. Based on the position vectors x and X the metric matrices g_{ij} and G_{ij} can be derived for the deformed and the undeformed configuration, respectively. Subsequently, the components of the Green's strain tensor in a local frame of reference $\bar{t}^i$ are set up according to:

$$\gamma_{kl} = \frac{1}{2}[g_{ij} - G_{ij}]t_k^i t_l^j. \tag{3}$$

The local frame of reference is determined by the orientation of a characteristic material axis (e.g. fibre orientation) and the shell thickness director D which leads to the factors t_k^i in eq.(3). After some algebra the Green's strain tensor can be written as a function of the displacement field u. When the interpolation of the displacement field is introduced, the components of the Green's strain tensor can be rewritten as a function of the nodal displacements.
To derive the stiffness matrix of the element the equilibrium in the weak form is established. After some algebra the stiffness matrix K of the solid-like shell element and the internal force vector can be derived. For a detailed description the reader is referred to [4, 12].

2.2 *Interface element*

To describe physically nonlinear effects like cracking and delamination interface elements have been applied. Interface elements are elements of zero thickness which are inserted into the finite element mesh at locations where cracking or delamination are expected to occur. In Figure 4 interface elements are displayed that can be combined with the sixteen-noded solid-like shell element, and in particular the twelve-noded interface element is displayed in Figure 5. The constitutive relation of interface elements is set up between the relative displacements v of the two adjacent layers of the interface elements and the tractions t in the interface. The relative displacement between the adjacent layers in a material point of the interface element can be written as:

$$v = RLBu_g = B_g u_g \tag{4}$$

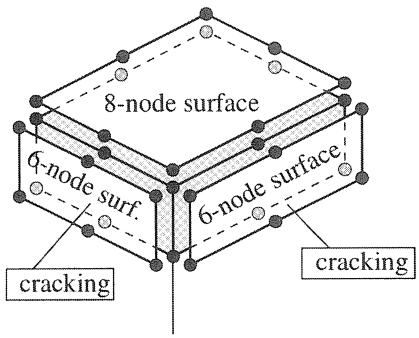

Fig. 4. Location of the interface elements for the sixteen-noded solid-like shell element.

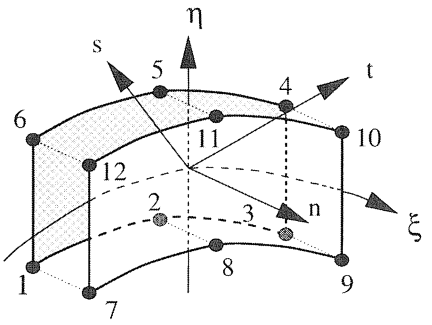

Fig. 5. Geometry of the twelve-noded interface element.

In eq.(4) the matrix $\boldsymbol{R}$ denotes the rotation matrix from the global into the local frame of reference. The latter is defined in every material point of the interface element by the two tangential directions and the normal direction of the layer, Figure 5. The matrix $\boldsymbol{L}$ is a mapping matrix which maps the displacements of the adjacent layers onto their relative displacements. The matrix $\boldsymbol{B}$ contains the shape functions which are dependent on the isoparametric variables ξ and η. The vector $\boldsymbol{u}_g$ contains the nodal displacements of the interface element. When the equilibrium is established in the weak form, the stiffness matrix $\boldsymbol{K}$ and the internal force vector f_{in} of the interface element can be derived:

$$\boldsymbol{K} = \int_{\xi}\int_{\eta} \boldsymbol{B}_g^T \boldsymbol{D} \boldsymbol{B}_g \ \det J_0 \mathrm{d}\xi \mathrm{d}\eta \qquad \text{and:} \qquad f_{in} = \int_{\xi}\int_{\eta} \boldsymbol{B}_g^T \boldsymbol{t} \ \det J_0 \mathrm{d}\xi \mathrm{d}\eta \tag{5}$$

In eq.(5) the matrix $\boldsymbol{D}$ represents the material stiffness matrix and J_0 the Jacobian. In the elastic regime the interface element represents a perfect bond between the adjacent layers. This is achieved by using a high dummy stiffness.

3 Residual strength analysis of centre cracked plates made of GLARE

3.1 *Interface crack model*

The use of interface elements to describe cracking introduces new degrees of freedom. Cracking occurs when a critical parameter, e.g. often the principal normal stress or critical *K*-factors, exceeds a certain threshold value. Then, a new degree of freedom is created at this node yielding a geometrical discontinuity. With interface elements cracking can occur between elements only and is therefore dependent on the original orientation of the finite elements. Since the direction of the crack growth is known due to experimental observations the discrete crack model combined with interface elements is a good approach to evaluate crack propagation [9, 14].

In interface elements the constitutive relation is set up between the relative displacements and the tractions in the interface. For the formulation of constitutive relation which governs the material behaviour and the description of the physically nonlinear effects different approaches are described

in the literature. Depending on the failure mechanisms for which the interface elements are applied the mathematical formulation can be based on an explicit traction/displacement relation [13], on a phenomenological plasticity approach [15] or on a damage theory [1].
When cracking is described with interface elements the assumption of a perfect bond between the two adjacent layers must be modified. In a general situation all three traction components in the plane of cracking contribute to the initiation of a crack. For a fully open crack this means that no stress can be transferred in any of the three directions in the plane of cracking, even under single-mode loading. To account for this effect a loading function f is now introduced. This loading function bounds all states of traction in the interface. Inelastic deformations occur when a state of traction violates the loading function. For the present model these inelastic deformations represent the crack opening in a material point. In the limiting state of a fully open crack the loading function shrinks to a point in the origin of the traction space. This implies that no load can be transferred in the material point, not even in compression. The loading function f reads:

$$f(\boldsymbol{t}, \kappa) = \sqrt{\frac{3}{2}\boldsymbol{t}^{\mathrm{T}}\boldsymbol{P}\boldsymbol{t}} - \bar{t}(\kappa) \leq 0; \qquad \text{with:} \qquad \boldsymbol{P} = \begin{bmatrix} \frac{2}{3} & 0 & 0 \\ 0 & 2 & 0 \\ 0 & 0 & 2 \end{bmatrix} \tag{6}$$

In eq.(6), the quantity $\bar{t}$ denotes the equivalent traction and the matrix $\boldsymbol{P}$ is set up with reference to von Mises plasticity. The shape of the loading function is given in Figure 6. When a state of traction violates the loading function a return-mapping algorithm must be applied which maps the state of traction back onto the surface of the loading function while the inelastic deformations grow. Then, the relative displacement increment is decomposed into an elastic part and an inelastic part, which gives:

$$\Delta \boldsymbol{v}_{\mathrm{n+1}} = \Delta \boldsymbol{v}^{\mathrm{el}}_{\mathrm{n+1}} + \Delta \boldsymbol{v}^{\mathrm{cr}}_{\mathrm{n+1}} \tag{7}$$

Applying an associative flow rule the incremental crack opening deformations v^{cr} can be written as:

$$\Delta \boldsymbol{v}^{\mathrm{cr}}_{\mathrm{n+1}} = \Delta \lambda_{\mathrm{n+1}} \left(\frac{\partial f}{\partial \boldsymbol{t}} \right) \Big|_{\mathrm{n+1}} \tag{8}$$

In eq.(8) $\Delta\lambda$ represents the finite amount of inelasticity and the gradient $(\partial f / \partial \boldsymbol{t})$ sets the direction of the crack opening deformations. The increment of the elastic relative displacements Δv^{el} is related to the traction increment $\Delta \boldsymbol{t}_{\mathrm{n+1}}$ at the end of the loading step via the linear elastic stiffness matrix $\boldsymbol{D}$:

$$\Delta \boldsymbol{v}^{\mathrm{el}}_{\mathrm{n+1}} = \boldsymbol{D}^{-1} \Delta \boldsymbol{t}_{\mathrm{n+1}} \tag{9}$$

Upon substitution of eq.(7) and eq.(8) into eq.(9) we obtain the traction increment which finally leads to the tractions:

$$\boldsymbol{t}_{\mathrm{n+1}} = \boldsymbol{t}_0 + \Delta \boldsymbol{t}_{\mathrm{n+1}} = \boldsymbol{t}_{\mathrm{trial}} - \Delta \lambda_{\mathrm{n+1}} \boldsymbol{D} \left(\frac{\partial f}{\partial \boldsymbol{t}} \right); \qquad \text{with:} \qquad \boldsymbol{t}_{\mathrm{trial}} = \boldsymbol{t}_0 + \boldsymbol{D} \Delta \boldsymbol{v}_{\mathrm{n+1}} \tag{10}$$

If the trial traction $\boldsymbol{t}_{\text{trial}}$ violates the loading function, eq.(6), the corresponding tractions and the crack opening deformations are calculated according to:

$$\boldsymbol{t}_{n+1} - \boldsymbol{t}_{\text{trial}} + \Delta\lambda_{n+1}\boldsymbol{D}\left(\frac{\partial f}{\partial \boldsymbol{t}}\right) = 0; \qquad \text{and:} \qquad f(\boldsymbol{t}_{n+1}, \kappa_{n+1}) = 0 \tag{11}$$

The latter two equations represent a system of four equations with five unknowns: $\boldsymbol{t}$, κ, $\Delta\lambda$. For the final solution of eq.(11) a hardening hypothesis must be introduced which sets the relation between $\Delta\lambda_{n+1}$ and $\Delta\kappa_{n+1}$. Applying eq.(11) and the hardening hypothesis $\Delta\kappa = f(\Delta\lambda)$ the loading function f can be rewritten as a function of $\Delta\kappa$ only [5]. Starting with $\Delta\kappa_0 = 0$ a new $\Delta\kappa$ can be calculated applying a Newton-Raphson procedure which reads:

$$\Delta\kappa_{n+1}^{k+1} = \Delta\kappa_{n+1}^{k} - \frac{f}{df/d\Delta\kappa}\Big|_{n+1}^{u} \tag{12}$$

Subsequently, the new $\Delta\lambda$ and new tractions $\boldsymbol{t}$ are computed [5].

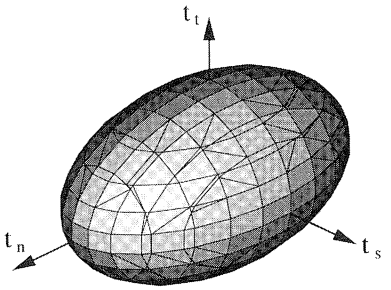

Fig. 6. Surface of the loading function applied with interface elements to describe cracking.

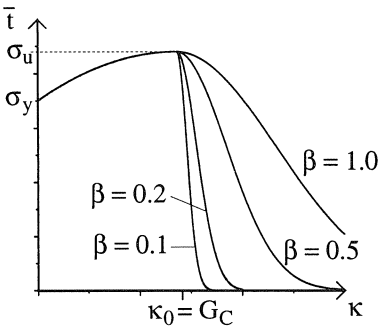

Fig. 7. Equivalent stress as function of the softening parameter κ.

3.2 *Hardening hypothesis*

For the derivation of the return-mapping algorithm, a modified work hardening hypothesis is applied which reads in an incremental manner:

$$\Delta\kappa_{n+1} = \Delta\lambda_{n+1} t^{T}\left(\frac{\partial f}{\partial t}\right) \tag{13}$$

The computed $\kappa = \kappa_0 + \Delta\kappa$ can directly be compared with the fracture toughness G_c of the material.

3.3 *Function of the equivalent traction*

Similar to the traction-separation law by Tvergaard and Hutchinson [17] the function $\bar{t}(\kappa)$ is a phenomenological representation of the fracture process and not a description of the atomic separation. In the present model the fracture process is initialised when the yield stress σ_y is reached. Upon further loading the stress increases from the yield stress σ_y up to the ultimate stress σ_u of the material, Figure 7. When the ultimate stress is reached the plastic work per unit surface area equals the critical fracture toughness G_C of the material. At this point the crack is fully opened and the dissipated energy equals the fracture energy. The stress has been reduced to zero while the inelastic relative displacements continue to grow. To obtain a smooth transition from the hardening to the softening branch, the hardening regime is described by a quadratic function:

$$\bar{t} = -\frac{\sigma_u - \sigma_y}{G_C^2}\kappa^2 + 2\frac{\sigma_u - \sigma_y}{G_C}\kappa + \sigma_y \tag{14}$$

and the softening regime is described by an exponential function:

$$\bar{t} = \sigma_{res} + (\sigma_u - \sigma_{res})e^{k}; \qquad \text{with:} \qquad k = -\left(\frac{\kappa - G_C}{\beta G_C}\right)^2 \tag{15}$$

The parameter β determines the rate of softening. For a sharp decrease $\beta = 0.5$ is chosen.
The hardening and softening branch are shown schematically in Figure 7. The residual stress σ_{res} is a small value ($\sigma_{res} = 10^{-2} MPa$) in order to achieve numerical stability for the return-mapping algorithm. Next to the return-mapping algorithm the consistent tangent stiffness matrix is applied to assure efficient and stable numerical simulations [5].

3.4 *Centre cracked plate made of GLARE™*

In the following the behaviour of a centre cracked plate made of GLARE™ is studied. The width of the plate equals 400 mm and its length is 800 mm. Due to geometrical symmetry and material symmetry only one quarter of the plate is modelled with sixteen-noded solid-like shell elements. At the symmetry line, starting from the crack tip onwards interface elements are located. Here, the displacements in the i_1-direction of one plane of the interface elements (in Figure 8 the right plane) are restrained. In the i_2-direction the displacements of both planes of the interface elements are equal. Thus, pure mode-I cracking is enforced. The plate is loaded with a distributed load as depicted in Figure 8. The material parameters for GLARE™ and the interface crack model are given by Hashagen et al. [7]. Plasticity in the plate is accounted for by an anisotropic plasticity model [8] which has been applied with a yield stress $\sigma_{11}^{(tension)} = 320 MPa$ and $\sigma_{11}^{(tension)} = 360 MPa$, respectively.
In Figures 9 and 10 the crack length extension and the crack mouth opening displacement of the centre cracked plate are displayed. From these graphs we can conclude that the numerical results

obtained with the interface crack model agree well with the experimental results [18]. Depending on the yield stress σ_{11} the computed ultimate loading lies within a range of five percent of the experimental value $\sigma_{gross} = 319\ MPa$.
In Figure 11 the distribution of the normal traction is visualised for the interface elements which are located along the i_2-axis of the model, see Figure 8. The load levels refer to the external loads (a)–(d) which are marked in Figure 9. We observe that the stress decreases sharply when the ultimate stress of the material is reached. The distribution of the dissipated energy is visualised in Figure 12.
The location of the sharp growth of the dissipated energy again coincides with the location of the ultimate stress in the traction profile. This position indicates the location of the crack tip which is displayed in Figure 10. Due to the choice of the exponential softening function, in which the equivalent stress does not become zero, the traction in the interface remains at a small residual value in the fully cracked situation. Due to imperfections in the plate buckling is observed in most of the experiments. Here buckling is understood as a movement of material points out of the plane in which the plate is located. In the experiments buckling can prevented by so-called anti-buckling guides. To compare experimental and numerical results when anti-buckling guides are not mounted to the plate an imperfection is applied to the finite element model. For this purpose an out-of-plane force is imposed on the cracked plate prior to the inplane loading. The small force $P = 0.05N$ which triggers buckling acts on the plate at the centre of the crack, point A in Figure 8.
In Figure 13 the crack length extension is visualised. Again, we observe that the calculated crack length extension agrees well with the experimental values. Especially, the residual strength of the plate matches with the experimental value. Also, the rate of crack growth calculated in the numerical analysis agrees with the experimental observations. In Figure 14 the gross stress is displayed as a function of the out-of-plane displacement of point A. It can be observed that the load at the onset of buckling calculated in the numerical analysis agrees with the experimental value. The dissipated energy and the traction profile in the interface elements show the same characteristics as for the plate without buckling. In Figure 15 the deformed state of the cracked plate is displayed for the load levels $\sigma_{gross} = 250 MPa$ of the pre-peak regime and the post-peak regime, respectively. The out-of-plane displacement is clearly visible and has a maximum value at the centre of the crack (point A).

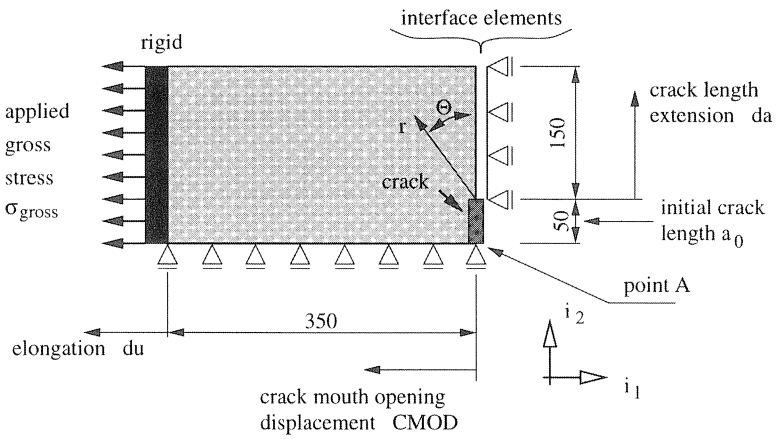

Fig. 8. Geometrical properties (in [mm]) and boundary conditions of the centre cracked plate with a thickness 1.4 mm that is made of GLARE™ .

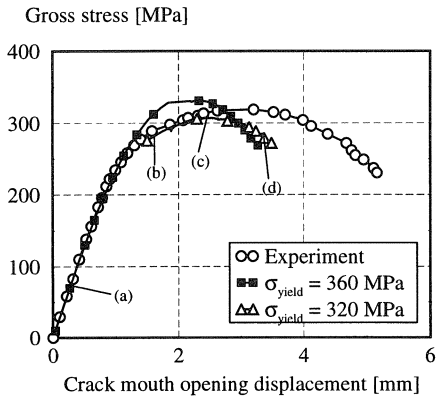

Fig. 9. Gross stress versus crack mouth opening displacement of the centre cracked plate made of GLARE™.

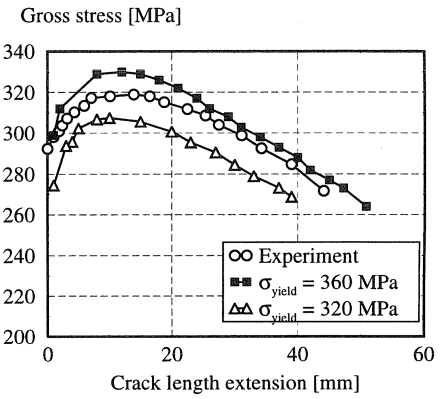

Fig. 10. Gross stress versus the crack length extension of a centre cracked plate made of GLARE™ .

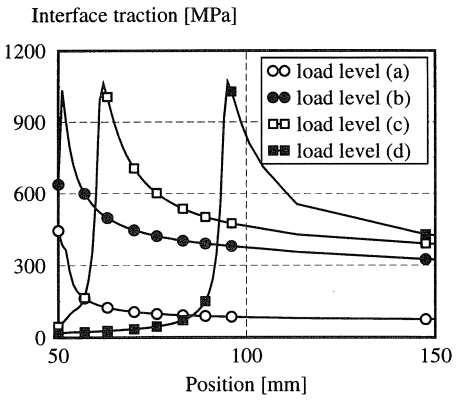

Fig. 11. Distribution of the normal traction in the interface of the centre cracked plate madc of GLARE™ for different load levels.

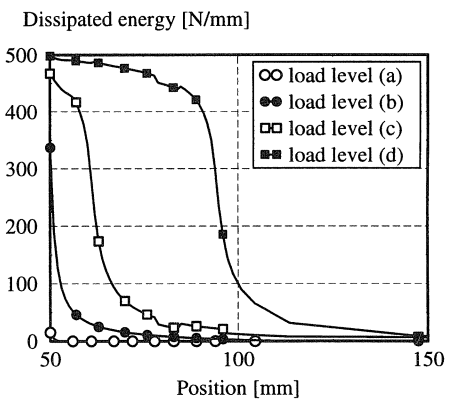

Fig. 12. Distribution of the dissipated energy in the interface of the centre cracked plate made of GLARE™ for different load levels.

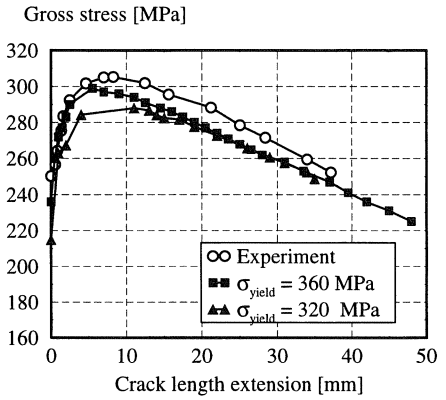

Fig. 13. Gross stress versus crack length extension of the centre cracked plate made of GLARE™ with an imperfection.

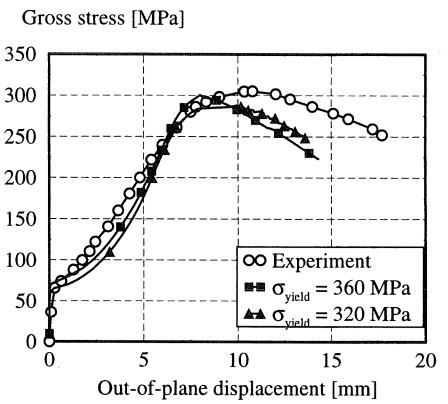

Fig. 14. Gross stress versus out-of-plane displacement of the centre cracked plate made of GLARE™ with an imperfection.

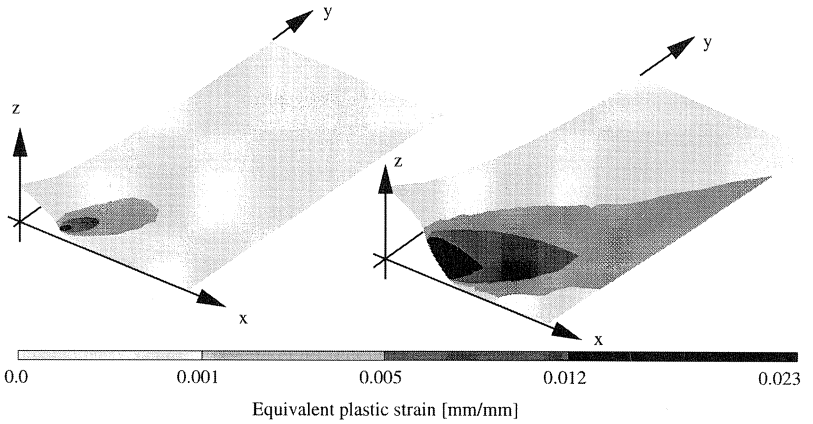

Fig. 15. Deformed configuration and equivalent plastic strain of the GLARE™ plate with imperfection for a gross stress of 250 MPa: left: pre-peak loading, right: post-peak loading.

4 Delamination analysis of spliced tension specimen made of GLARE™

4.1 Introduction to the splicing concept

As a benefit of the layered composition of fibre metal laminates the splicing technique can be applied to increase the width of the fibre metal laminate sheets. The width of the aluminium layers is limited due to production aspects. But two or more aluminium layers can be connected by bridging prepreg layers which reduces the weight of the constructions for which fibre metal laminates are applied. In Figure 16 the principle of the splicing technique is displayed. The gaps

between the aluminium layers are filled with resin to avoid moisture contact. In the remaining, the aluminium layer which forms the gap is denoted as broken, and the layers which remain intact at the gap are denoted as bridging layers. As a result of the gap in the broken aluminium layer the load must be transferred to the prepreg layer and the aluminium layer that bridge the gap. Therefore, the interface between the broken aluminium layer and the bridging prepreg layer is loaded considerably. For high load levels the bond between the aluminium and the prepreg layer can become too weak. In the limiting case the bond disappears totally, the aluminium layer and prepreg layer are separated and delamination occurs, see Figure 17. For the description of delamination in composites various models and different concepts are detailed in the literature [1, 2, 11, 16]. Ladeveze and Allix introduce a damage parameter which describes the degradation of the stiffness of the interface upon loading. König and Krüger compute the mixed mode energy release rates and compare it with a critical energy release rate. In the present study the phenomenological approach by Schellekens and de Borst [16] is followed.

4.2 *Numerical formulation of the delamination model*

Similar to the interface crack model a loading function bounds all states of traction in the material point. If a state of traction violates the loading function, delamination is initialised. Then, the state of traction is mapped back onto the loading surface while the inelastic deformations grow.
The material parameters describing the loading function are the tension strength $\bar{t}_t$, the compression strength $\bar{t}_c$ and the two shear strengths of the interface $\bar{t}_{si}$. The growth of the delamination is described with the fracture toughness G_C. In the limiting case when the energy dissipated by the inelastic deformations equals the fracture toughness of the material a fully delaminated area has occurred in the material point. The loading function f_{id} for delamination in the interface is displayed in Figure 18 and reads:

$$f_{id}(\boldsymbol{t}, \kappa) = \frac{1}{2}\boldsymbol{t}^T \boldsymbol{P}_{id}\boldsymbol{t} + \boldsymbol{t}^T \boldsymbol{q}_{id} - \bar{t}^2(\kappa); \tag{16}$$

with:

$$\boldsymbol{P}_{id} = \mathrm{diag}\left[2, \frac{2}{(\bar{t}_1)^2}, \frac{2}{(\bar{t}_2)^2}\right], \qquad \boldsymbol{q}_{id}^T = [\bar{t}_c - \bar{t}_s(\kappa), 0, 0]; \tag{17}$$

and:

$$\bar{t}^2 = \bar{t}_c \bar{t}_t s(\kappa); \qquad \bar{t}_\alpha = \frac{\bar{t}_{s\alpha}}{\sqrt{\bar{t}_t \bar{t}_c}} s(\kappa) \qquad \alpha = 1, 2. \tag{18}$$

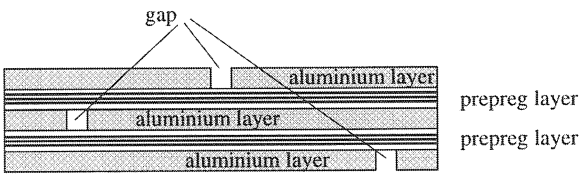

Fig. 16. Schematic sketch of a splice.

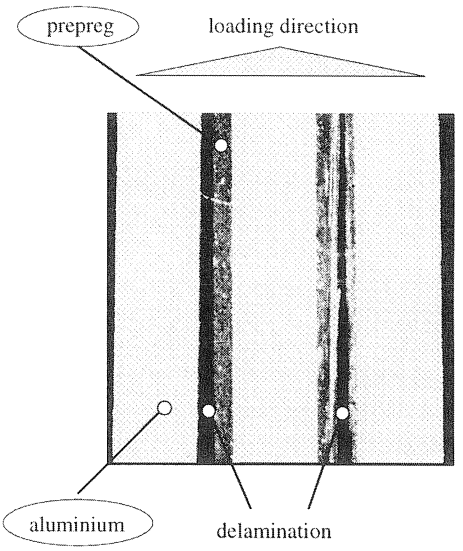

Fig. 17. Delamination of a spliced specimen.

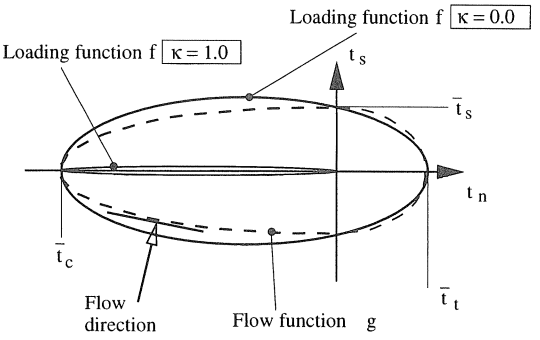

Fig. 18. Loading function and plastic potential of the delamination model.

In the limiting state when a material point has delaminated totally, shear tractions cannot be transferred anymore. Therefore also the shear strengths $\bar{t}_\alpha$ depend on the softening parameter κ. Since the compressive strength is not affected by softening, for total delamination all states of traction are located on a straight line between the compressive strength and zero. The function $s(\kappa)$ is linear with $s(0) = 1$ and $s(G_C) = 0$.

If a state of traction violates the loading function ($f_{id} < 0$) a local return-mapping algorithm is carried out. As a result the state of traction is mapped back onto the loading surface and the inelastic deformations grow. Similar to the interface crack model the relative displacements are decomposed into an elastic part Δv^{el} and an inelastic part Δv^{id}.

Here a non-associative flow rule is applied to avoid numerical problems [6]. The plastic potential from which the flow direction is derived consists of two regimes for positive and negative tensile

tractions, respectively. They differ in the set-up of the mapping matrix $\hat{\boldsymbol{P}}_{\mathrm{id}}$. Thus, the inelastic relative displacement equals:

$$\Delta v^{\mathrm{er}}_{n+1} = \Delta\lambda_{n+1}\left(\frac{\partial f}{\partial t}\right)\Big|_{n+1} \qquad ; \text{with} \qquad g_{\mathrm{id}} = \frac{1}{2}\boldsymbol{t}^{\mathrm{T}}_{n+1}\hat{\boldsymbol{P}}_{\mathrm{id}}(\kappa_{n+1})\boldsymbol{t}_{n+1} \tag{19}$$

and

$$\hat{\boldsymbol{P}}_{\mathrm{id}} = \mathrm{diag}\left[\frac{2}{(\bar{t}_{\mathrm{t}S})^2}, \frac{2}{(\bar{t}_{\mathrm{s}1S})^2}, \frac{2}{(\bar{t}_{\mathrm{s}2S})^2}\right] \qquad \text{for a positive normal traction;} \tag{20}$$

$$\hat{\boldsymbol{P}}_{\mathrm{id}} = \mathrm{diag}\left[\frac{2}{(\bar{t}_{\mathrm{c}})^2}, \frac{2}{(\bar{t}_{\mathrm{s}1S})^2}, \frac{2}{(\bar{t}_{\mathrm{s}2S})^2}\right] \qquad \text{for a negative normal traction.} \tag{21}$$

When the modified work hardening hypothesis eq.(13) is applied the return-mapping algorithm and the tangent stiffness matrix can be derived. These algorithms are similar to those of the crack model. They are elaborated and described in detail by Hashagen et al. [6].

4.3 *Delamination in spliced tension specimen*

To assess the behaviour of fibre metal laminates in the presence of splices two different configurations of spliced specimen are considered. The first configuration is composed of three aluminium layers and two prepreg layers. In this configuration two splices are located in the two outer aluminium layers. It is referred to as doubly spliced. The geometry and the boundary conditions of the finite element model for this design are displayed in Figure 19. The second configuration is referred to as asymmetrically spliced and consists of two aluminium layers with only one prepreg layer. Here, the splice is located in one of the outer aluminium layers. The geometry and the boundary conditions for this specimen are also displayed in Figure 19. The thickness of the aluminium layer equals t = 0.5 mm and the thickness of the prepreg layer is 0.125 mm. By virtue of symmetry only one quarter of every configuration needs to be modelled with solid-like shell elements. Moreover, the mid-surface of the doubly spliced specimen can be used as symmetry plane for a further reduction of the finite element model. In the experiments a reference length of 50 mm is used to calculate the strain. The splice is located in the middle of this reference length, see Figure 19.

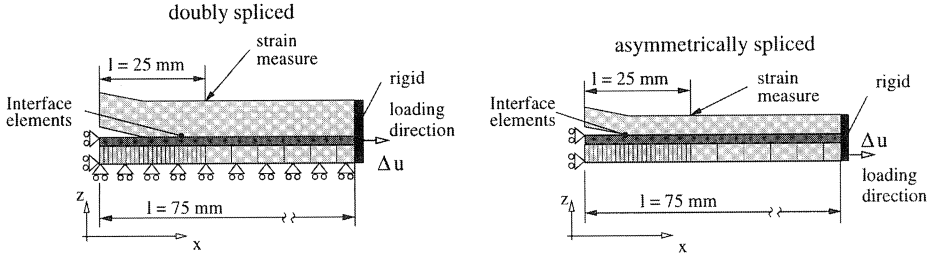

Fig. 19. Geometry and boundary conditions of the doubly spliced specimen (left) and the asymmetrically splice specimen (right).

The material data for the aluminium, the prepreg and the interface are given by Hashagell et al. [6]. Hereby, the fracture toughness of the material has been determined by various experiments (de Vries et al.[19]). In the present study a fracture toughness $G_C = 1.1$ N/mm is used.
In the following, specimens are analysed in which the fibres in the prepreg are oriented in the loading direction. The applied load is represented by the gross stress σ_{gross} which is the total load divided by the unspliced cross area (12.5 mm $\times$ t_{total}) of the specimen. The components of the traction are referred to the x-, y- and z-direction of the global frame of reference, Figure 19. The dissipated energy can be decomposed into three components which also refer to the x-, y- and z-direction of the global frame of reference.
In Figure 20 the stress-strain curve is displayed for the doubly spliced specimen with $t_{alu} = 0.5$ mm and fibres oriented in the loading direction. The gross stress is also plotted versus the delamination length, Figure 21. In the numerical model the delamination is initialised when the state of traction first violates the loading function f_{jd}. Then, the delamination process starts and energy dissipates. However, not all energy is dissipated at once. Therefore, material points in the specimen appear for which delamination has just started and others which are fully delaminated. To assess the impact of this process on the delamination length three different curves are plotted in Figure 21. The first curve is obtained for the position where delamination is initialised ($\kappa = 0.0$ N/mm). The second curve marks the position where fifty percent of the fracture toughness is dissipated ($\kappa = 0.5G_C$) and the third curve marks the position of the fully delaminated material points. It can be concluded that the strain and the delamination length calculated numerically show a good agreement with the experimental results, although the numerical analysis gives a slightly higher ultimate load.

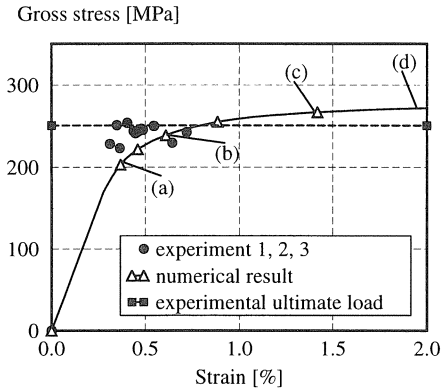

Fig. 20. Gross stress versus strain for the doubly spliced specimen.

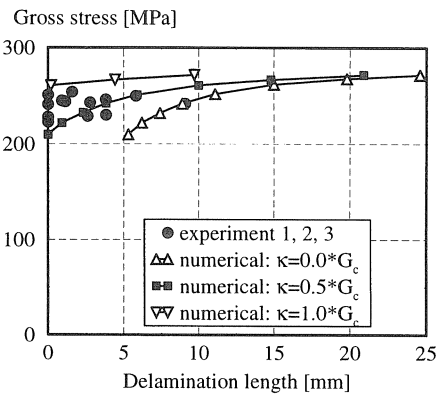

Fig. 21. Gross stress versus delamination length for the doubly spliced specimen.

In Figures 22–24 the normal traction and the two shear tractions, t_z, t_x and t_y are visualised for the load levels (a)–(d) which are marked in Figure 20. We observe that the peak of the traction components propagates in the x-direction when the load and subsequently the delamination length increase. In the region which has been passed by the delamination front the tractions decrease again to a near zero state. The shear traction component t_y which is oriented perpendicular to the loading direction increases significantly at the free edge of the specimen in the region where delamination is

initialised. This behaviour can be explained by considering the different lateral contractions of the layers which are loaded and which are unloaded when the delamination front propagates through the material. Due to the difference of the lateral contraction a relative displacement between the layers which bridge the splice and the broken layer is initialised. Consequently, a shear traction perpendicular to the loading direction is observed.

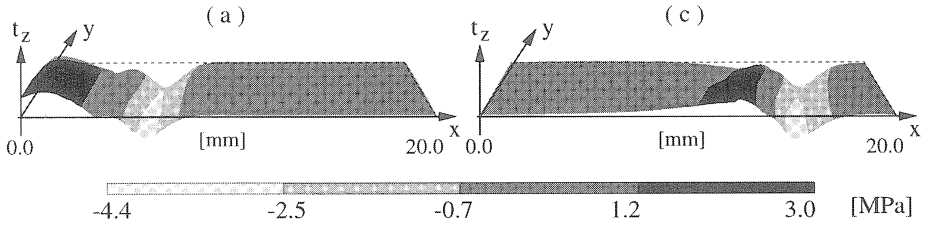

Fig. 22. Traction profile in the z-direction in the interface of the doubly spliced specimen.

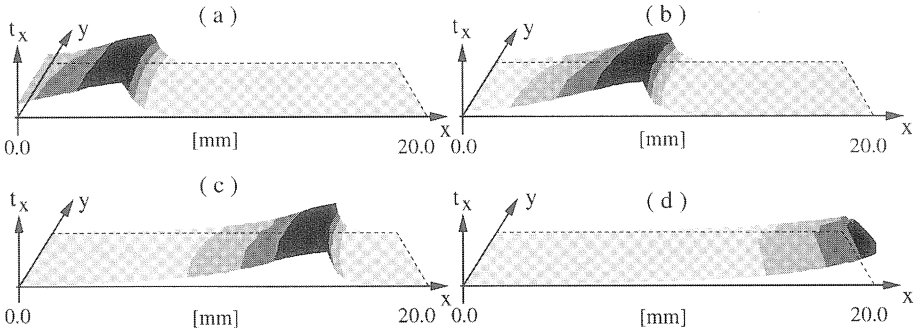

Fig. 23. Traction profile in the x-direction in the interface of the doubly spliced specimen.

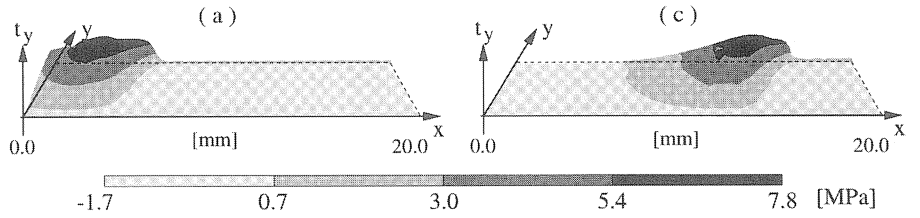

Fig. 24. Traction profile in the y-direction in the interface of the doubly spliced specimen.

The dominant role of the shear component in the loading direction is also emphasised when the dissipated energy is studied. In Figures 25 - 27 the energy is displayed which is dissipated in the normal direction and the two shear directions, *z*-, *y*- and *x*-direction, respectively. In Figure 26 we

observe that the energy dissipated in the z-direction of the model (normal direction of the interface) is less than the energy dissipated in the x- and y-directions which form the two shear components of the interface. Furthermore, the zone where energy is dissipated in the z-direction is restricted to the tip of the splice and does not grow in the x-direction when the specimen is loaded, see Figure 26. In contrast to this observation we can see that the zone where energy is dissipated in the x-direction and in the y-direction grows when loading the specimen. In particular, the energy which is dissipated in the x-direction of the specimen is much larger than the energy dissipated in the y-direction. In the centre of the specimen the x-component of the dissipated energy reaches nearly the fracture toughness of the interface. However, at the free edge of the specimen a significant y-contribution to the dissipated energy can be noticed. Similar to the traction component, the differences in the lateral contraction between the bridging layers and the broken layer are responsible for the energy dissipation in the y-direction. When delamination occurs the bridging layers are loaded further while the broken layer unloads. This induced difference in the displacement of the layers results in a considerable energy dissipation.

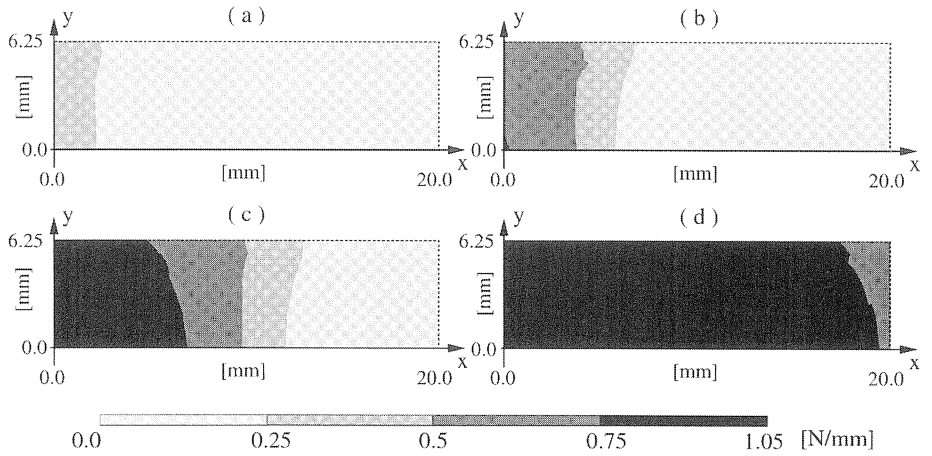

Fig. 25. Dissipated energy in the x-direction in the interface of the doubly spliced specimen.

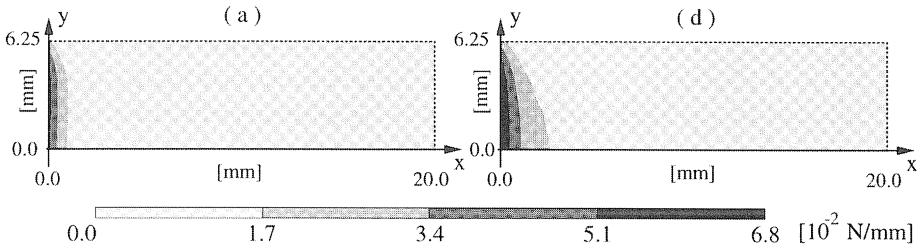

Fig. 26. Dissipated energy in the z-direction in the interface of the doubly spliced specimen.

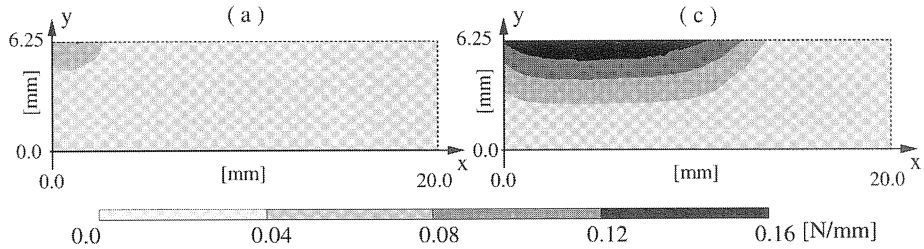

Fig. 27. Dissipated energy in the y-direction in the interface of the doubly spliced specimen.

4.4 *Asymmetrically spliced specimen*

The asymmetrically spliced specimen is analysed in the same manner as the doubly spliced specimen, but now the aluminium layer is 0.3 mm thick. For the asymmetrically spliced specimen the assumption of a geometrically linear behaviour has a strong impact on the results and leads to a significant difference between numerical and experimental data. In Figures 28 and 29 the displacement of the tip of the splice in the z-direction is displayed versus the applied load. The two graphs are obtained assuming a geometrically linear formulation and a geometrically nonlinear formulation respectively. Obviously, the displacement in the z-direction grows steadily when a geometrically linear behaviour is assumed. In contrast, for the geometrically nonlinear formulation the displacement in the z-direction passes a maximum and decreases slightly afterwards. In the present calculation the maximum displacement is approximately 0.12 mm. The out-of-plane displacement in the z-direction can be explained with the location of the neutral axis of the specimen. Except for the region around the splice, the neutral axis of the specimen is located in the middle of the prepreg layer which is also, for this region, the symmetry line of the specimen. At the splice, however, one of the two aluminium layers is broken and the lay-up is not symmetric anymore with respect to the original neutral axis. Thus, at the splice the neutral axis of the specimen is located in the bridging aluminium layer. When the specimen is loaded the difference of the positions of the neutral axis gives the maximum displacement of the bridging section in the z-direction. For the given geometry the maximum displacement is not higher than $u_z = 0.15$ mm. In Figure 30 the gross stress is displayed versus the strain and in Figure 31 versus the delamination length for geometrically nonlinear and geometrically linear formulation of the applied finite elements. Here, the differences between geometrically linear and geometrically nonlinear formulation lead to a significant difference in the numerically calculated delamination length. For the geometrically linear formulation a larger delamination length is computed. This length differs from the experimentally measured delamination length. The latter matches with the numerically calculated delamination length when a geometrically nonlinear behaviour is assumed. The formulation of the finite elements, either geometrically linear or geometrically nonlinear, has a serious impact on the delamination process computed in the numerical analysis. In Figure 32 the energy is displayed which is dissipated in the z-direction of the specimen (mode-I). Again, the geometrically linear and nonlinear cases are considered. The load levels (a) and (b) refer to a gross stress $\sigma_{gross} = 250$ MPa and $\sigma_{gross} = 340$ MPa, respectively, see Figure 30. Two major differences are noticed when the results obtained with the two formulations are analysed. First, the total energy which is dissipated in the z-direction is more

than four times higher for the geometrically linear formulation compared with that of the geometrically nonlinear formulation. Secondly, the zone where energy is dissipated in the z-direction is larger for the geometrically linear formulation than for the geometrically nonlinear formulation. In Figure 33 the energy which is dissipated in the x-direction (mode-II) is visualised for the geometrically linear and for the geometrically nonlinear formulation. Again, the load levels (a) and (b) refer to the external forces σ_{gross} = 250 MPa and σ_{gross} = 340 MPa, see Figure 30. We observe that the dissipated energy is larger for the geometrically linear formulation than for the geometrically nonlinear formulation. Furthermore, the maximum of the dissipated energy in x-direction is not located at the tip of the splice as for the geometrically nonlinear formulation. Finally, at the free edge of the specimen less energy is dissipated in the x-direction for the geometrically linear formulation compared with the centre of the specimen.

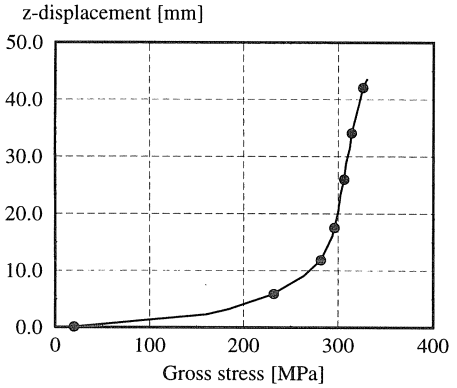

Fig. 28. Displacement in the z-direction of the tip of the splice for geometrically linear behaviour.

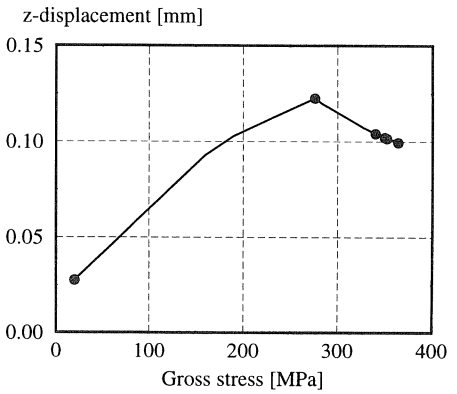

Fig. 29. Displacement in the z-direction of the tip of the splice for geometrically nonlinear behaviour.

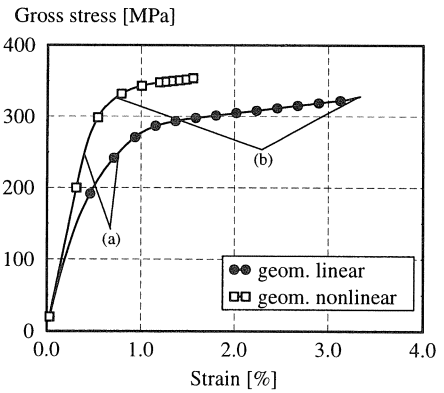

Fig. 30. Gross stress versus strain of the asymmetrically spliced specimen with t_{alu} = 0.3 mm.

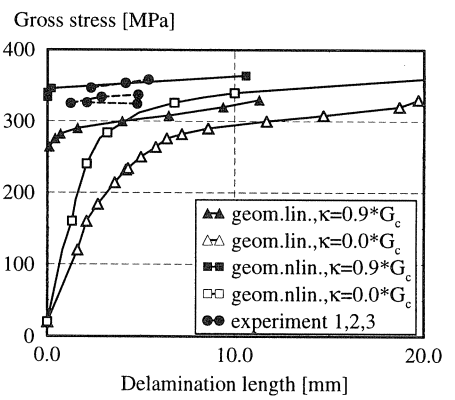

Fig. 31. Gross stress versus delamination length of the asymmetrically spliced specimen with t_{alu} = 0.3 mm.

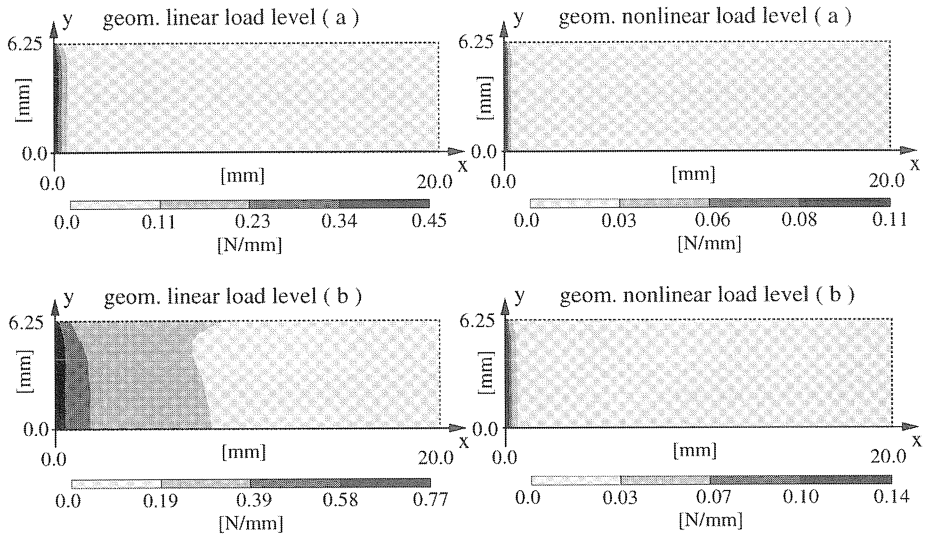

Fig. 32. Dissipated energy in the z-direction in the interface of the asymmetrically spliced spccimen.

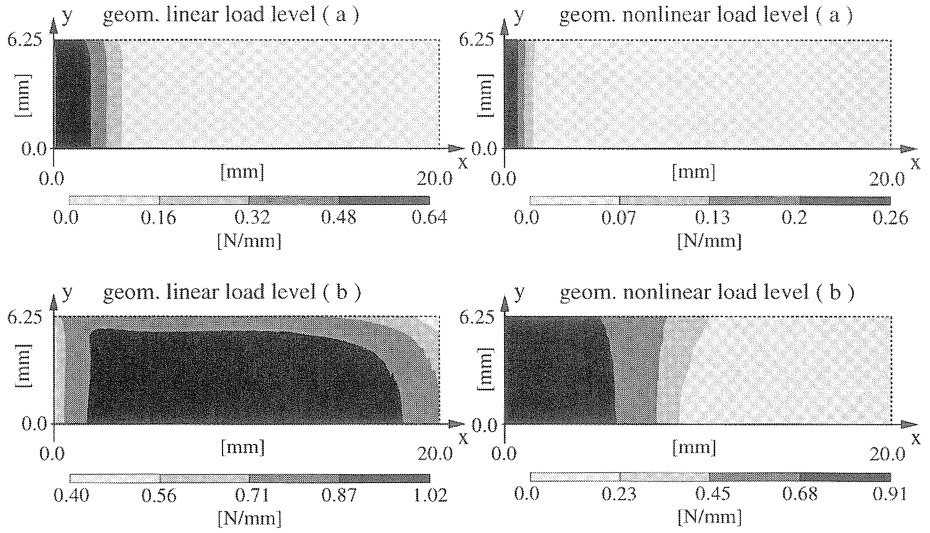

Fig. 33. Dissipated energy in the x-direction in the interface of the asymmetrically spliced specimen.

5 Conclusions

In the present paper a numerical strategy has been introduced to describe crack propagation and delamination propagation in fibre metal laminates. The strategy has been based on a solid-like shell element and corresponding interface elements. The interface elements have been located in the finite element mesh at positions where either cracking or delamination is expected to occur. Cracking and delamination have been accounted for by the introduction of loading functions which bound all states of traction in the interface. When a state of traction violates the loading function a return-mapping algorithm is carried out to map the state of traction back onto the surface of the loading function. Due to this process energy is dissipated. When the dissipated energy equals the fracture toughness a fully cracked or fully delaminated area occurs.
The numerical models have been applied successfully to a residual strength analysis of centre cracked plates made of GLARE™. Here, the numerical results show a good agreement with the experimental data. Especially, the residual strength of the plate and the rate of crack growth has been represented correctly. Furthermore, the calculated out-of-plane displacement of a centre cracked plate with imperfection agrees with the experimental observations. The material data which serve as input for the numerical model have been derived from theories that are applied for homogeneous material. Thus, the good agreement between experimental and numerical results justifies the application of these theories for fibre metal laminates.
Finally, delamination in spliced tension specimen made of GLARE™ has been studied. Here, it has been found that mode-II delamination plays a dominant role in the delamination process. A noteworthy contribution of mode-I delamination occurs only at the tip of the splice and only for the initialisation of delamination. It appeared that geometrically nonlinear behaviour must be taken into consideration for the asymmetrically spliced tension specimen. For the delamination analysis too, the numerical models have led to a better understanding of the delamination process in fibre metal laminates.

References

[1] Allix O. and Ladeveze P., Modelling and computation of delamination for composite laminates, *Arch. Mech.*, **44**, 5-13 (1992)

[2] Corigliano A., Formulation, identification and use of interface models in numerical analysis of composite delamination, *Int. J. Sol. Struct.*, **30**(20), 2779-2811 (1993)

[3] Bischoff M. and Ramm E., Shear deformable shell elements for large strains and rotations, *Int. J. Numer. Meth. Engng.*, **40**, 4427-4449 (1997)

[4] Hashagen F., A geometrically and physically nonlinear layered solid-like shell element, *TU Delft report nr.: 03-21-0-31-22*, Delft University of Technology, Delft, The Netherlands, (1995)

[5] Hashagen F., An interface element for crack modelling in aluminium, *TU Delft report nr. 03-21-0-31-22*, Delft University of Technology, Delft, The Netherlands (1996)

[6] Hashagen F., Borst R. de and Vries T. de, Delamination behaviour of spliced fibre metal laminates, part II: numerical investigation, *Int. J. Comp. Struct.*, (submitted for publication)

[7] HASHAGEN F., BORST R. DE, Modelling onset and growth of mixed-mode cracking in fibre metal laminates, *Proc. 4th World Cong. Comp. Mech.*, (to appear)

[8] HASHAGEN F., BORST R. DE, A plasticity model including anisotropic hardening and softening for composite materials, in: *Finite Elements in Engrg. and Scien. Proc. 2nd Int. DIANA Conf.* eds.: HENDRIKS M.A.N., JONGEDIJK H., ROTS J.G., VAN SPANJE W.J.E. and BLAKMA, A.A. Rotterdam, The Netherlands, pp. 1139-1147 (1997)

[9] HOHBERG J.-M., A joint element for the nonlinear dynamic analysis of arch dams, *Dissertation*, ETH Zürich, Zürich, Switzerland (1992)

[10] HORST P. and OHRLOFF N., Possible application of GLARE material as shown by the example of the AIRBUS A330, *Proc. Deutsch. Luft- und Raumfahrtkongreß 1994 - DGLR-Jahrestagung*, ed.: Bürgener G., Erlangen, Germany, 591-600, (1994)

[11] KÖNIG M. and KRÜGER R., Computation of energy release rates: a tool for predicting delamination growth in carbon fibre reinforced epoxy laminates, *Proc. 4th Int. Conf. Compu. Plast. COMPLAS IV*, eds. OWEN D.R.J., HINTON E. and OÑATE E., Pineridge Press, Swansea, U.K., 1167-1178 (1995)

[12] PARISCH H., A continuum-based shell theory for non-linear applications, *Int. J. Num. Meth. Engrg.*, **38** (11), 1855-1833 (1995)

[13] ROTS J.G., Computational modeling of concrete fracture, *Dissertation*, Delft University of Technology, Delft, The Netherlands (1988)

[14] ROTS J.G. and SCHELLEKENS J.C.J., Interface elements in concrete mechanics, in: *Computer Aided Analysis and Design of Concrete Structures*, eds.: Bicanic N., Mang H., Pineridge Press, Swansea, Wales, UK, 909-918 (1990)

[15] SCHELLEKENS J.C.J., Computational strategies for composite structures, *Dissertation*, Delft University of Technology, Delft, The Netherlands (1992)

[16] SCHELLEKENS J.C.J., and BORST R. DE, Free edge delamination in carbon-epoxy laminates: a novel numerical/experimental approach, *Compo-. Struct.*, **28**, 357~373 (1994)

[17] TVERGAARD V. and HUTCHINSON J.W., The influence of plasticity on mixed mode interface toughness, *J. Mech. Phys. Solids*, **41**(6), 1119-1135 (1993)

[18] VRIES T. DE, Various parameters concerning the residual strength of aircraft materials, part II: test data and charts, *Graduation thesis*, Delft University of Technology (1994)

[19] VRIES T. DE, VLOT A., HASHAGEN F., Delamination behaviour of spliced fibre metal laminates, part I: experimental results, *Int. J. Comp. Struct.*, (submitted for publication)